Graphical Abstract

CFD modeling of sewage sludge combustion in an experimental entrained flow reactor with integrated slag flow dynamics

Benjamin Ortner, Laura Peham, Christian Schmidberger, René Prieler, Christoph Hochenauer

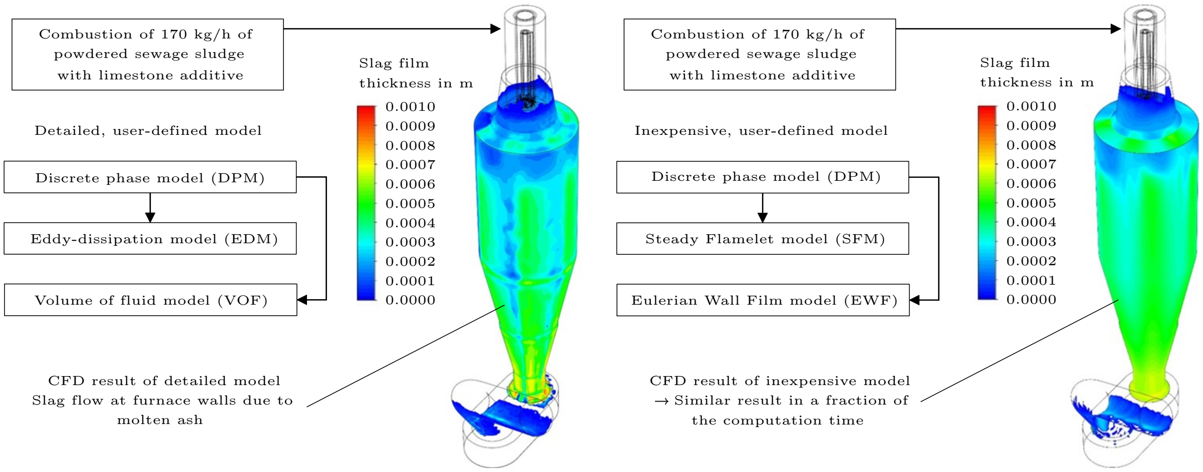

Highlights

CFD modeling of sewage sludge combustion in an experimental entrained flow reactor with integrated slag flow dynamics

Benjamin Ortner, Laura Peham, Christian Schmidberger, René Prieler, Christoph Hochenauer

- First application of UDF-based, 3D slag flow CFD model in sewage sludge combustion
- A new, computationally inexpensive approach is developed as an alternative
- New model predicts slag flow similarly but cuts computation time by 95%.
- Detailed slag flow simulation using both models, featuring a complex geometry
- Study highlights balance between computational efficiency and model accuracy

CFD modeling of sewage sludge combustion in an experimental entrained flow reactor with integrated slag flow dynamics

Benjamin Ortner[a], Laura Peham[a], Christian Schmidberger[b], René Prieler[a], Christoph Hochenauer[a]

[a] *Institute of Thermal Engineering, Faculty of Mechanical Engineering and Economic Sciences, Graz University of Technology, Inffeldgasse 25B, 8010 Graz, Austria*

[b] *Institute of Combustion and Power Plant Technology, Faculty 4 - Energy-, Process- and Bio-Engineering, University of Stuttgart, Pfaffenwaldring 23, 70569 Stuttgart, Germany*

Abstract

This study addresses the important role of slag flow predictions in sewage sludge combustion systems. From the typically high ash content, valuable elements such as phosphorus can be recovered. Two advanced computational fluid dynamics (CFD) modeling approaches are evaluated in terms of their predictive capabilities. A sophisticated Eddy Dissipation Model/Volume of Fluid (EDM/VOF) approach serves as the state-of-the-art benchmark for evaluating a novel Steady Diffusion Flamelet/Eulerian Wall Film (SFM/EWF) method. Both models feature user-defined coupling with the discrete phase model (DPM) and show general agreement on the evolution and final characteristics of the slag flow on the walls of a newly developed entrained flow reactor. With an input of 170 kg/h of sludge, the models predict a maximum slag thickness of approximately 0.6 to 1.0 mm and a maximum slag flow velocity of about 37 mm/s. It was found that the slag flow is mostly unaffected by the swirling gas and follows a pattern primarily driven by gravity. In summary, the straightforward SFM/EWF method can deliver high-quality predictions at a fraction of the computational cost compared to the EDM/VOF approach. It generates statistically steady slag flow results in less than two days on a standard workstation, significantly faster than the 35-day minimum required by the EDM/VOF model. This speed-up is achieved through reduced mesh requirements and fewer transport equations. The paper also highlights the limitations of this computationally efficient model regarding film growth normal to the walls, a critical aspect in freeze-lining applications.

Keywords:

Sewage sludge combustion, Slag flow, Computational fluid dynamics

1. Introduction

The European Commission has designated phosphorus as a critical raw material due to the European Union's heavy reliance on imports of this essential element. The primary source countries for phosphorus imports are

Email address: `benjamin.ortner@tugraz.at` (Benjamin Ortner)

China, Vietnam, and Kazakhstan [1, 2]. To mitigate this dependency, a circular economy approach, such as recycling sewage sludge - which contains significant amounts of phosphorus - offers a potential solution. However, since sewage sludge also contains various harmful substances, thermal treatment followed by phosphorus recovery from combustion residues (ash), as demonstrated in the *FlashPhos* process [3], presents a promising option [4, 5].

Given the complexity of industrial-scale plants, there is a strong demand for advanced tools in research, development, and engineering. Understanding the flow phenomena within these devices requires insight beyond chemical equilibrium considerations, which can only be provided by 3D-CFD models. While models for entrained flow reactors, such as the Flash reactor in the FlashPhos process, can be adapted from those used in coal combustion and gasification, sewage sludge has distinct characteristics that differ significantly from coal and biomass combustion. As a result, novel modeling approaches are necessary. Additionally, given the limitations of computational resources, these models should also be computationally efficient.

1.1. Sewage sludge combustion and modeling

Gao et al. provided a review on the thermochemical conversion of sewage sludge, describing its combustion behavior as similar to that of other solid fuels [6]. Compared to coal, there is a high occurrence of ash and a high volatile yield. In high-temperature environments, it was even found by Arnout et al. that the entire organic content can evaporate [7]. This is why sewage sludge combustion was even compared to that of gaseous fuels by Werther and Ogada [8, 9]. Furthermore, Cui et al. noted that drying and devolatilization can happen simultaneously [10], especially in high-heating rate environments. A significant difference to the combustion of coal is the high ash content in the fuel, which can reach up to 50%. This results in a low heating value of the material but also has substantial implications for the design of combustion reactors. The high ash content leads to slag flow due to molten ash, which can interact with the gas flow and influence the overall system dynamics. Additionally, the chemically aggressive nature of the slag has important implications for the refractory design, as it may cause degradation and damage to the reactor linings.

Žnidarčič et al. [11] proposed a surrogate combustion model for sewage sludge in small-scale incineration plants, which was later extended to include reduced chemical kinetics mechanisms [12]. Ortner et al. [13] leveraged the high volatile yield and rapid heating rate characteristic of entrained flow combustion of fine sewage sludge powder for computationally efficient CFD modeling. This approach incorporated a simplified surrogate model based on the steady diffusion flamelet model (SFM). In a subsequent study, Ortner et al. [14] explored ash-deposition behavior in

Nomenclature

Abbreviations

CFD	Computational fluid dynamics
CFL	Courant-Friedrichs-Lewy
DPM	Discrete phase model
DRW	Discrete random walk
EDM	Eddy dissipation model
EWF	Eulerian wall film
LHV	Lower heating value
PSD	Particle size distribution
SFM	Steady flamelet model
SIMPLE	Semi-implicit method f. pressure-linked equations
UDF	User-defined function
URANS	Unsteady Reynolds-Averaged Navier-Stokes
VOF	Volume of fluid
WSGGM	Weighted sum of grey gases model

Greek symbols

α	Volume fraction
ϵ	Emissivity
ε	Turbulence dissipation rate
λ	Thermal conductivity
ρ	Density
μ	Dynamic viscosity
ψ	Sphericity

Roman symbols

c_p	Specific heat (constant pressure)
d	Diameter
D	Film thickness
f	Mixture fraction
f'^2	Mixture fraction variance
g	Gravitational acceleration
h	Enthalpy
k	Turbulence kinetic energy
$\dot{m}$	Mass flow
p	Pressure
S	Source term
u_i, u_j, u_k	Velocity components
t	Time
x_i, x_j, x_k	Position
Y	Species mass fraction

Subscripts

ED	Eddy-dissipation
$fuel$	Surrogate fuel
g	Gas phase
ox	Oxidizer
P	Particle
s	Slag phase

a basic experimental furnace, though the study did not yet address the flow of slag along reactor walls, leaving room for further research. The behavior of the melt in a tundish can be simulated in a computationally efficient manner, as demonstrated by Ortner et al. [15, 16]. However, this approach has also not yet incorporated the modeling of slag flow along the furnace walls.

1.1.1. Slag flow modeling

For fuels with a high ash content, accurate modeling of the behavior of molten slag is crucial. However, in conventional coal combustion, the formation of molten slag typically occurs only at elevated temperatures, which can increase emissions such as NO_x. As a result, recent literature on CFD modeling that includes slag flow is relatively limited. Nevertheless, understanding slag flow is critical in specialized applications, where it is unavoidable or even desired. This includes devices like melting cyclones or the entrained flow combustion of sewage sludge, as described in this study. Key publications addressing the integration of slag flow into CFD models are briefly discussed below, with a comprehensive review provided by Bhuiyan et al. [17, 18].

In 1998, Seggiani [19] introduced the first one-dimensional, time-dependent slag model compatible with CFD codes. This model employed vertically arranged control volumes to simulate flow and heat transfer within the slag layer, focusing solely on vertical flow. By solving conservation equations for mass, momentum, and energy, the model determined flow distribution using an analytical expression for falling film flows. Inputs from CFD calculations - such as ash mass influx, gas temperatures, and heat flux - were used to predict the slag layer's surface temperature. Building on Seggiani's work, Benyon [20] developed what is believed to be the first two-dimensional slag model in 2002 that could be integrated with CFD codes. This model accounted for circumferential variations, including changes in slag layer thickness due to material deposition in a gasifier. However, the 2D expansion was implemented by treating multiple parallel instances of a 1D model independently, without interaction between adjacent sections. Notably, all the reviewed slag flow models operate under the assumption that the shear stress between the gas and the slag layer is negligible. In 2007, Liu and Hao [21] advanced the integration of slag layers into CFD simulations by employing the VOF model. Their 2D simulation focused on a small vertical section of a gasifier wall, introducing particle mass through a uniformly distributed source term. Xu et al. later developed a comprehensive multiphase reaction- and slag flow model, focusing on the refractory brick corrosion rate [22], a crucial aspect in the context of phosphorus recovery. However, their model did not resolve slag flow directly within the CFD framework but relied on a submodel approach. User-defined submodels that do not directly resolve slag flow with computational cells continue to be effectively coupled with gasification models today, as demonstrated by Chen et al. [23]. In 2013, Chen and Ghoniem introduced an innovative three-dimensional slag model to study slag behavior in a pressurized oxy-coal combustor [24, 25]. This approach combined the VOF model with the DPM, offering a detailed resolution of slag dynamics, including slag layer buildup, multiphase flow, and heat transfer processes. Their findings closely aligned with experimental observations, providing a valuable tool for the design and development of coal furnaces and gasifiers. Bhuiyan and Naser further demonstrated the applicability of the Eulerian Wall Film model for predicting slag flow [26, 27], successfully reproducing results from Chen et al. while utilizing a species transport approach in the form of the Eddy Breakup model. Jønck presented an advanced CFD model specifically designed for melting cyclones in his PhD thesis [28]. This work emphasizes the simulation of complex physical phenomena within the melting cyclone, including multiphase flow, combustion, phase changes, and radiation. The study featured several integrated and modified models, such as an adjusted EMD tailored for oxygen-enriched combustion, a model for tracking the melting of raw materials, and the coupling of the DPM with the VOF multiphase model.

In summary, highly capable and comprehensive 3D slag models are available, though they are often both complex and computationally expensive.

1.1.2. Objective of this study

The goal of this study is to evaluate and compare the predictive performance and limitations of two distinct modeling approaches: the advanced Eddy Dissipation Model/Volume of Fluid (EDM/VOF) method, which - to the best of our knowledge - is being implemented for the first time for the combustion of sewage sludge, and the novel SFM/EWF method presented in this study. These models are applied to simulate the slag flow in a newly developed entrained flow reactor (Flash reactor), thereby testing the models on a complex geometry. The study aims to demonstrate that the SFM/EWF method can deliver high-quality predictions at a lower computational cost and with greater stability, while also addressing the specific limitations of each model in capturing essential flow characteristics relevant to the process.

2. Flash reactor system, fuel material and operating conditions

The Flash reactor system can best be explained using Fig. 1, which illustrates its major components. The reactor is essentially a top-fired entrained flow reactor, featuring a water-cooled burner that injects pre-dried, powdered sewage sludge into a vertically oriented combustion chamber with an inner diameter of 1 m. Within the combustion chamber, a highly swirling flow is generated by the burner, creating an oxygen-enriched environment that promotes the combustion process and helps to reach high-enough temperatures. The reaction zone narrows into a conical part, directing flue gases into a phase separator zone. Molten ash accumulates on the furnace walls, forming a slag film, which is collected in a tundish (not shown) and eventually tapped. In this novel experimental reactor, sewage sludge is combusted and melted simultaneously. It is designed to facilitate variations in the sludge-additive mixture, excess air ratio, temperature levels and oxygen-enhancement levels.

It is expected that the majority of the slag is separated from the flue gas within the cylindrical and conical sections of the system. This is due to the flame-stabilizing swirl induced by the burner (details found in [29]), which directs particles that melt to droplets in-flight [30] toward the refractory walls, where they are deposited and form a film flow.

A proximate and elementary analysis of the sludge is given with Tab. 1. An ash analysis is found in Tab.

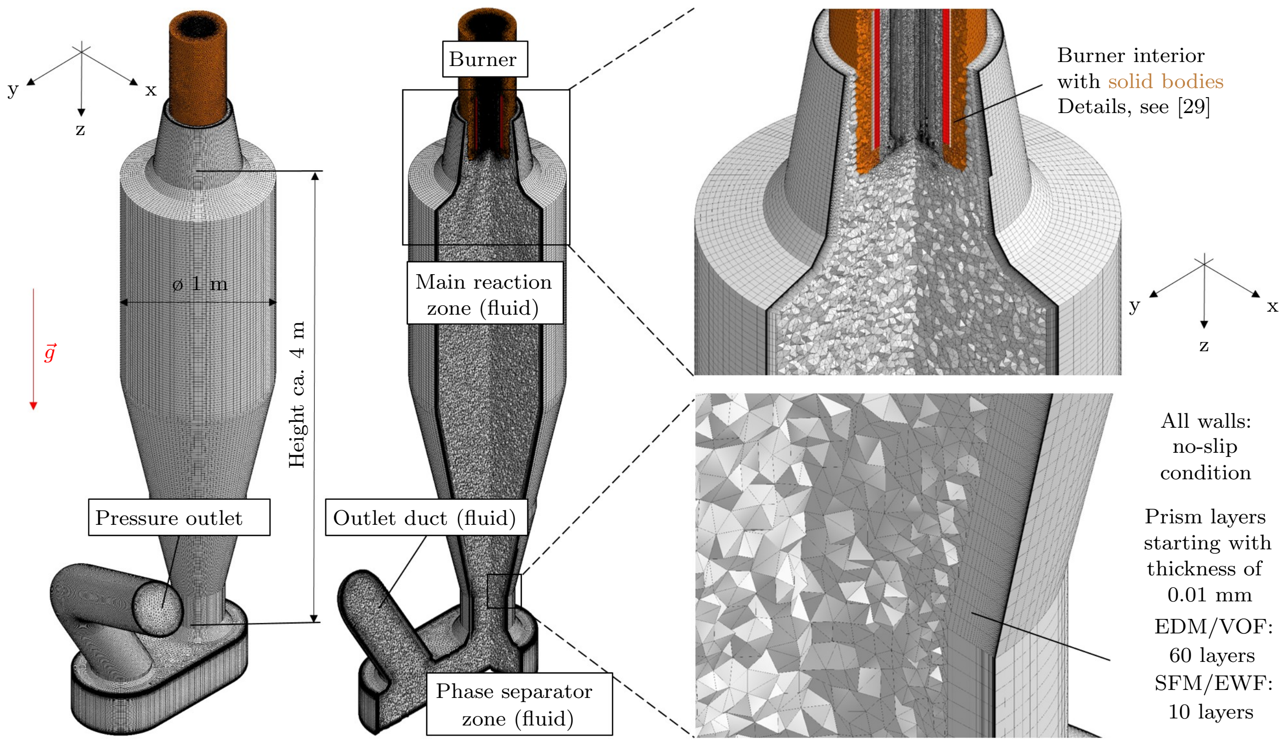

Figure 1: Considered Flash reactor system with computational mesh

2. It describes a sewage sludge that originates from Balingen, Germany that can be considered to be quite a typical example for the material. The particle size distribution (PSD) is taken from dynamic image analysis (DIA) measurements and can be described in a simplified manner using a Rosin-Rammler-PSD [31, 32] with $x' = 52.6e{-}06$ m as size- and $n = 1.137$ as spread parameter. A comparative simulation was performed with a PSD that features $x' = 142.6e - 06$ m as size- and $n = 1.067$ as spread parameter.

The addition of limestone is intended to modify the slag for further processing and to serve as a flux, as the CaO content of the slag mixture is increased after calcination in the furnace (reaction 1). Consequently, the slag viscosity at these elevated temperatures of approximately 1550°C-1600°C is estimated to be around 0.3 $Pa \cdot s$. Though, as shown in other studies [24, 25], this may vary significantly, depending on the sewage sludge composition, temperature and even furnace atmosphere [33]. For simplicity, a value of 0.3 $Pa \cdot s$ is also used in the simulations. The density is assumed to be constant with a value of 2100 kg/m$^{\mathbf{3}}$. The thermal conductivity was set to 1.1 $W/(m \cdot K)$; the surface tension estimate is 0.42 N/m [28]. Implications of varying slag material properties are discussed in the supplementary material document.

$$CaCO_3(s) \rightarrow CO_2(g) + CaO(s) \quad \Delta H_R = 168kJ/mol \tag{1}$$

Table 1: Sludge properties, ar = as received, daf = dry, ash-free

	Unit	Value
Proximate analysis (ar)		
LHV	MJ/kg	9.2
Moisture	wt %	10.0
Ash	wt %	45.0
Volatile matter	wt %	40.9
Fixed carbon	wt %	4.1
Ultimate analysis (daf)		
C	wt %	50.8
H	wt %	6.8
O	wt %	34.1
N	wt %	6.4
S	wt %	1.9

Table 2: Ash analysis (water- and organic free, 550°C)

Component	wt% as oxide
SiO_2	31.5
CaO	16.1
P_2O_5	14.2
Al_2O_3	16.7
Fe_2O_3	16.7
MgO	3.15
K_2O	1.68
Na_2O	-
SO_3	-

The system operates under mildly oxygen-enriched conditions to ensure temperatures above the solidification point, including within the phase separator zone. The mass flows of the fuel and oxidizer are detailed in Tab. 3. In total, the oxidizer includes 25vol% of O_2 at an excess air ratio of approximately 1.05. These values are also used as flow boundary conditions for the CFD simulations (turbulent intensity 5%).

3. Computational modeling

In this section, the computational modeling for two approaches is described. *ANSYS Fluent 2024R1* is used for all simulations performed within this study. Since the Flash reactor is a complex system that involves different multiphase aspects, the section is divided into the particle-laden flow, combustion, and slag flow descriptions. The explanation of the computational domain is followed by an outline of the solution procedure.

Table 3: Operating conditions

		Mole frac. in %	Mass flow in kg/h	Temperature in K
Oxidizer				
Carrying air	O_2	21.0	78.6	300
	N_2	79.0	258.9	300
O_2-enriched	O_2	36.4	48.3	300
air	N_2	63.6	73.8	300
Fuel / additive				
Sewage sludge		-	170	300
Limestone		-	17	300

3.1. Particle-laden reactive flow

At the core of the flow field computations are the Favre-averaged (˜) Navier-Stokes equations including continuity Eq. (2), momentum Eq. (3) and enthalpy Eq. (4). These equations incorporate source terms S, which account for particle-in-cell sources, chemical reactions, and slag deposition.

$$\frac{\partial \overline{\rho}}{\partial t} + \frac{\partial}{\partial x_i}(\overline{\rho}\tilde{u_i}) = S_m \tag{2}$$

$$\begin{aligned} \frac{\partial}{\partial t}(\overline{\rho}\tilde{u_i}) + \frac{\partial}{\partial x_j}(\overline{\rho}\tilde{u_i}\tilde{u_j}) = -\frac{\partial \overline{p}}{\partial x_i} + \frac{\partial}{\partial x_j}(\mu(\frac{\partial \tilde{u_i}}{\partial x_j} + \frac{\partial \tilde{u_j}}{\partial x_i})) \\ + \frac{\partial}{\partial x_j}(-\overline{\rho u_i' u_j'}) + \bar{\rho} g_i + S_{moment.} \end{aligned} \tag{3}$$

$$\frac{\partial}{\partial t}(\bar{\rho}\tilde{h}) + \frac{\partial}{\partial x_i}(\bar{\rho}\tilde{u_j}\tilde{h}) = \frac{\partial}{\partial x_i}(\frac{\lambda}{c_p}\frac{\partial \tilde{h}}{\partial x_i}) + S_{rad} + S_h \tag{4}$$

In Eq. (3), the unknown terms $\overline{\rho u_i' u_j'}$ are modelled using the Boussinesq hypothesis. The realizable $k-\varepsilon$ [34] is frequently employed due to its effectiveness in predicting swirling flows in combustion simulations [35–39]. Additional transport equations for the turbulence kinetic energy k, Eq. (5), and its dissipation rate ε, Eq. (6), have to be solved.

$$\begin{aligned} \frac{\partial}{\partial t}(\overline{\rho}k) + \frac{\partial}{\partial x_i}(\overline{\rho}k\tilde{u_i}) = \frac{\partial}{\partial x_j}\left[(\mu + \frac{\mu_t}{\sigma_k})\frac{\partial k}{\partial x_j}\right] \\ + G_k + G_b - \rho\varepsilon \end{aligned} \tag{5}$$

$$\frac{\partial}{\partial t}(\overline{\rho}\varepsilon) + \frac{\partial}{\partial x_j}(\overline{\rho}\varepsilon\tilde{u_j}) = \frac{\partial}{\partial x_j}\left[(\mu + \frac{\mu_t}{\sigma_\varepsilon})\frac{\partial \varepsilon}{\partial x_j}\right]$$
$$+\overline{\rho}C_1 S\varepsilon - \overline{\rho}C_2\frac{\varepsilon^2}{k+\sqrt{\nu\varepsilon}} + C_{1\varepsilon}\frac{\varepsilon}{k}C_{3\varepsilon}G_b \tag{6}$$

with $\mu_t = \overline{\rho}C_\mu k^2/\varepsilon$. The necessary definitions of the expressions (G_k, G_b, C_1, S, C_μ, $C_{3\varepsilon}$) and the values of the constants (σ_k, σ_ε, C_2, $C_{1\varepsilon}$) are described in Wu et al. [35].

An Euler-Lagrangian approach is used for the calculation of particle movement in the Flash reactor. The DPM is employed in this study. This model is appropriate as long as the volume fraction of particulate matter remains low [40]. According to digital image analysis measurements, the particles are slightly non-spherical (sphericity according to Wadell [41], $\psi \sim 0.8$), which is why the drag law from Haider and Levenspiel is applied. For the solution of the force balance in Eq. (7), the drag force F_D (Eq. (8)) is necessary. The values A-D for calculating the drag coefficient c_D are detailed in Haider and Levenspiel's publication [42].

$$\frac{du_P}{dt} = F_D\left(u - u_P\right) + \frac{g\left(\rho_P - \rho\right)}{\rho_P} \tag{7}$$

$$F_D = \frac{18\mu}{\rho_P d_P^2}\frac{c_D Re_P}{24} \tag{8}$$

$$c_D = \frac{24}{Re_P}\left(1 + A Re_P^B\right) + \frac{C}{1+\frac{D}{Re_P}} \tag{9}$$

The particle Reynolds number Re_P is defined using the relative velocity as given in Eq. (10)

$$Re_P = \frac{\rho d_P |u_P - u|}{\mu} \tag{10}$$

In some cases, it was noted in the literature that only detailed, fully transient large eddy simulations (LES) calculations were able to predict deposition rates at furnace walls with sufficient detail [14, 43, 44]. However, in this study, a large enough centrifugal force on the particles is provided by the swirling flow, so that realistic deposition patterns were predicted with URANS. Instead, Chen highlighted the necessity to include a stochastic model in the consideration [24, 25]. This is done in the form of the discrete random walk (DRW) model.

The Ranz-Marshall correlation for the Nusselt number [45] was considered sufficient for heat transfer, supported by both the literature [46–48] and the fact that this study focuses on small particles with shapes that closely approximate a sphere. The enthalpies for melting and calcination are included in the respective temperature-dependent specific heat curves of the sludge- and limestone particles. They are linked to the model inside the particle heat transfer Eq. (11) via a UDF.

$$m_P c_P \frac{dT_P}{dt} = h A_P \left(T_\infty - T_P\right) + \epsilon_P A_P \sigma \left(\Theta_R^4 - T_P^4\right) \tag{11}$$

h is the heat transfer coefficient, T_∞ the gas temperature, A_P the particle surface and σ denotes the Stefan-Boltzmann constant. In combustion simulations, radiation is an important aspect to consider [49]. Because of the relatively small and complex geometry of the system, the discrete ordinate method was used to solve the radiative transfer equation [50]. For the radiative properties of the gas, the weighted sum of grey gasses (WSGGM) model [51] - using coefficients from Smith et al. [52] - is applied. Furthermore, particle-radiation interaction is considered and accounted for. In Eq. (11), $\Theta_R = \left(\frac{G}{4\sigma}\right)^{\frac{1}{4}}$ is the radiation temperature, where G represents the incident radiation as calculated using the DO model. An emissivity of $\epsilon_P = 0.8$ is assigned to the particles.

3.2. Combustion modeling

During their flight through the domain, the particles undergo a devolatilization reaction, which can be quite complex for sewage sludge. For the reasons outlined in section 1.1, a single-step reaction [53] with kinetic parameters similar to that of lignite [40] is used ($E_a = 7.4e+07$ J/kmol and $A = 312,000$ 1/s). These values produced realistic results as shown in our previous comparisons with experiments [13, 14]. In the current version of *ANSYS Fluent* only the standard eddy-dissipation model (EDM) by Magnussen and Hjertager [54] can be coupled with the multiphase model necessary for the implementation of slag flow. The gas phase reactions are modeled as source terms R_i in the species transport equation Eq. (12), together with other sources S_i (devolatilization, char burnout).

$$\frac{\partial \rho Y_i}{\partial t} + \nabla \cdot (\rho u Y_i) = -\nabla \cdot J_i + R_i + S_i \tag{12}$$

J_i is the diffusion flux of species i obtained using the dilute approximation (Fick's law). The reactions are assumed to be mainly mixing-limited due to fast chemistry at high temperatures. The reaction rate R_{ED} is calculated using Eq. (13).

$$R_{ED} = A\rho\frac{\varepsilon}{k}\min\left[min\left[Y_{fuel},\frac{Y_{ox}}{\nu'_{ox}}\right],B\frac{\Sigma_p Y_{prod}}{\Sigma_j^N \nu''_j M_{w,j}}\right] \tag{13}$$

Here, A and B are empirical constants (Magnussen coefficients), left at default values. The first min-function, representing non-premixed combustion, is oriented around the smallest mass fraction Y of either the fuel or the oxidizing species divided by its stoichiometric coefficient ν'_{ox}. The second min-term represents the premixed case that is proportional to the product mass fractions Y_{prod} divided by the sum of their molar weights $M_{w,j}$ times their stoichiometric coefficients ν''_j. R_{ED} is compared to a kinetically determined rate R_{kin} of Eq. (14), with pre-exponential factor A, E_a and concentrations C,. The solver chooses the one that is smaller (Eq. (15)). Therefore, this approach is also known as the finite-rate/eddy dissipation model.

$$R_{kin} = AT^b\exp\left(-\frac{E_a}{RT}\right)\prod_{j=1}^{n}(C_j)^{e_j} \tag{14}$$

$$R = \min\left[R_{ED}, R_{kin}\right] \tag{15}$$

A simple, two-step mechanism is used for the combustion of volatiles released from the discrete particles during devolatilization. Therein, a single species *vol* with averaged properties and a standard enthalpy of formation of $-1.25e+08$ J/kg is used. The stoichiometric coefficients of reaction (16) are determined from the proximate and elementary analysis of the sludge. In a second step (Reaction (17)), the carbon monoxide is further oxidized to CO_2. The kinetics for reaction (16) are assumed very fast, reaction (17) uses data from Howard et al. [55].

$$\begin{aligned} vol + 0.797O_2 \longrightarrow 1.144CO + 1.114H_2O+ \\ 0.075N_2 + 0.020SO_2 \end{aligned} \tag{16}$$

$$CO + \frac{1}{2}O_2 \longrightarrow CO_2 \tag{17}$$

After the devolatilization process is finished, a char oxidation step is implemented, using a diffusion-limited approach (binary diffusivity 5e-04 m^2/s, oxidizing species O_2). Since not all particles are guaranteed to complete their devolatilization and char burnout process before being deposited at a furnace wall, a wall-burning model had to be considered. In this study, particles in touch with a furnace wall or slag surface are halted and allowed to continue to burn out at a by a factor of 0.5 reduced rate. It was achieved using a DPM-property UDF. This is done because it is assumed, that the particle is to some degree submerged in the slag surface, leading to a smaller surface area available for the chemical reaction.

While the parameters for particle devolatilization and char burnout are the same for all models in this study, the consideration of gas phase chemistry is an important distinction. For the computationally inexpensive alternative provided by our study, we use the SFM, which is a mixture-fraction (Eq. (18), Z_i refers to the elemental mass fractions for element i) based approach. This approach allows the implementation of a relatively detailed chemical reaction mechanism. In this study, the *heptane42.che* by Bui Pham et al. [56] is applied. It features 42 reversible reactions and involves 17 species, compared to the 2 reactions in the EDM approach with six species. Limitations of the SFM are discussed in [36].

$$f = \frac{Z_i - Z_{i,ox}}{Z_{i,fuel} - Z_{i,ox}} \tag{18}$$

Only two transport equations for the Favre-averaged mean mixture fraction $\bar{f}$ (Eq. (19)) and its variance $\overline{f'^2}$ (Eq. (20)) have to be solved.

$$\frac{\partial}{\partial t}\left(\rho \bar{f}\right) + \nabla \cdot \left(\rho \vec{v} \bar{f}\right) = \nabla \cdot \left(\frac{\mu_t}{\sigma_t} \nabla \bar{f}\right) + S_m \tag{19}$$

$$\begin{aligned} \frac{\partial}{\partial t}\left(\rho \overline{f'^2}\right) + \nabla \cdot \left(\rho \vec{v} \overline{f'^2}\right) = \nabla \cdot \left(\frac{\mu_t}{\sigma_t} \nabla \overline{f'^2}\right) \\ + C_g \mu_t \left(\nabla \bar{f}\right)^2 - C_d \rho \frac{\varepsilon}{k} \overline{f'^2} \end{aligned} \tag{20}$$

Here, μ_t is the turbulent viscosity, σ_t is the Prandtl number and S_m is used to consider the particle-related source term. For the remaining constants C_g and C_d, default values of 2.86 and 2.0 were retained. Reaction data is pre-calculated and stored in probability-density function (PDF) look-up tables, significantly reducing the necessary computation times.

3.3. Slag flow

This section outlines two approaches for modeling film flow, namely the VOF and EWF methods, following an initial estimation of film behavior within the Flash furnace. The estimation is based on the film Reynolds number, which indicates that the film flow along the reaction chamber walls is laminar.

3.3.1. Estimation of film properties

1D-correlations for laminar falling film flows are common in basic literature. The velocity profile of a laminar film flow is given in Eq. (21).

$$u(y) = \frac{gD^2\rho}{\mu}\left[\frac{y}{D} - \frac{1}{2}\left(\frac{y}{D}^2\right)\right] \tag{21}$$

Therein, $u(y)$ denotes the velocity at a distance y from the wall, however, this correlation still depends on the film thickness D. A simple integration step leads to an estimate for film thickness depending on a given mass flow in Eq. (22), wherein L is the width of the wetted surface, ignoring the curvature of the geometry.

$$D(\dot{m}, L) = \sqrt[3]{\frac{3\dot{m}\mu}{\rho^2 gL}} \tag{22}$$

If it is assumed that 60% of the injected slag mass is trapped at the reactor walls, this relates to 52 kg/h of relevant slag mass flow. With the material properties from section 2, Eq. (22) gives a maximum film thickness of 0.66 mm and in turn a maximum velocity of 14 mm/s using Eq. (21). The film Reynolds number in Eq. (23) can be used to get an estimate of the general flow properties.

$$Re = \frac{u_{avg}D\rho}{\mu} \tag{23}$$

Since this value is of the order of magnitude of 1e-02, significantly below the critical value of 4, the film flow can be expected to be laminar.

3.3.2. VOF modeling

The volume of fluid (VOF) model is employed due to the expected presence of well-defined interfaces between the slag and gas phases. The continuity equation Eq. (24) for the volume fraction α_s is then solved:

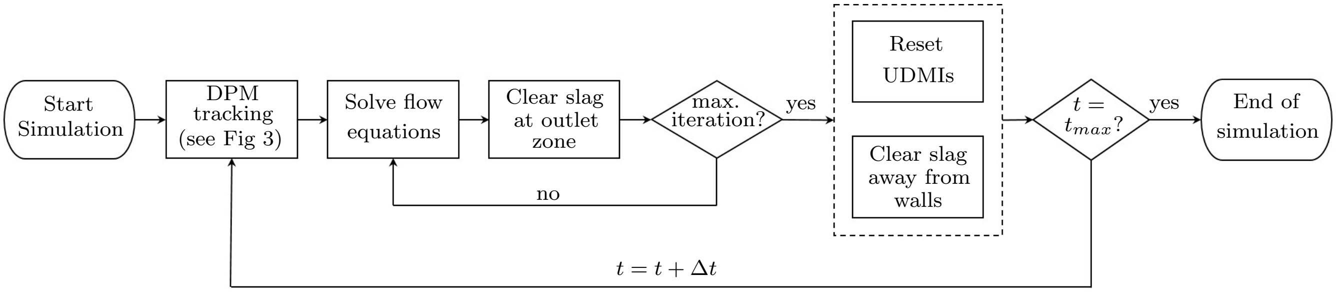

Figure 2: DPM-flow coupling

$$\frac{1}{\rho_s}\left[\frac{\partial}{\partial t}(\alpha_s \rho_s) + \nabla \cdot (\alpha_s \rho_s u_i)\right] = S_m \tag{24}$$

The subscript s denotes the consideration of the slag phase, so $\alpha_s = 1$ indicates that a cell is filled with slag whereas a value of zero means the cell contains only gas. If in a cell, $0 < \alpha_s < 1$, this indicates that the cell contains the interface between the phases, which is of high interest. Using the VOF model, one set of flow equations (2)-(6) is solved for all phases. The influence of the turbulence model being active also in the slag zone, e.g., close to the wall, is minimal (see supplementary material). The volume fraction of the primary phase (gas) is computed using the constraint that all phases must sum up to unity. The coupling between the DPM and VOF models is the most challenging aspect of the EDM/VOF approach. While the DPM model interacts with the flow mostly through the standard implementation in *ANSYS Fluent*, some modifications have been made, as shown in Fig. 2. Major instabilities were traced to small, non-zero slag volume fractions being re-entrained into the main flow region. To address this, a routine was implemented that removes any non-zero slag fractions far from the wall at each time step. Additionally, since slag dripping into the phase separator is irrelevant to this study, the slag phase fraction is reset to zero after every iteration. Both modifications are executed using *execute commands* within *Fluent*.

The core DPM tracking required extensive modifications, as illustrated in Fig. 3. Much of the routine builds on the work of Jønck [28], including the use of a modified drag law UDF for more accurate deposition modeling in slag-filled regions. Particle capture criteria follow the approach by Yong et al. [57], utilizing the Weber number and particle temperatures that are compared to critical values (see Tab 4). For small particles, the particle temperatures are closely related to the degree of conversion. As detailed in section 3.2, a wall-burning model was implemented since some particles remain unconverted upon impact with the walls. If deposition criteria are satisfied and the particle has burnt out, user-defined memories (UDM) store the mass and enthalpy sources for the next time step.

Table 4: Particle-wall interaction regime according to Yong et al. [57]

	Sticky particle		Non-sticky particle	
	$We < We_{cr}$	$We > We_{cr}$	$We < We_{cr}$	$We > We_{cr}$
Sticky wall	Slagging		Slagging	Reflect
Non-sticky wall	Fouling	Reflect	Reflect	

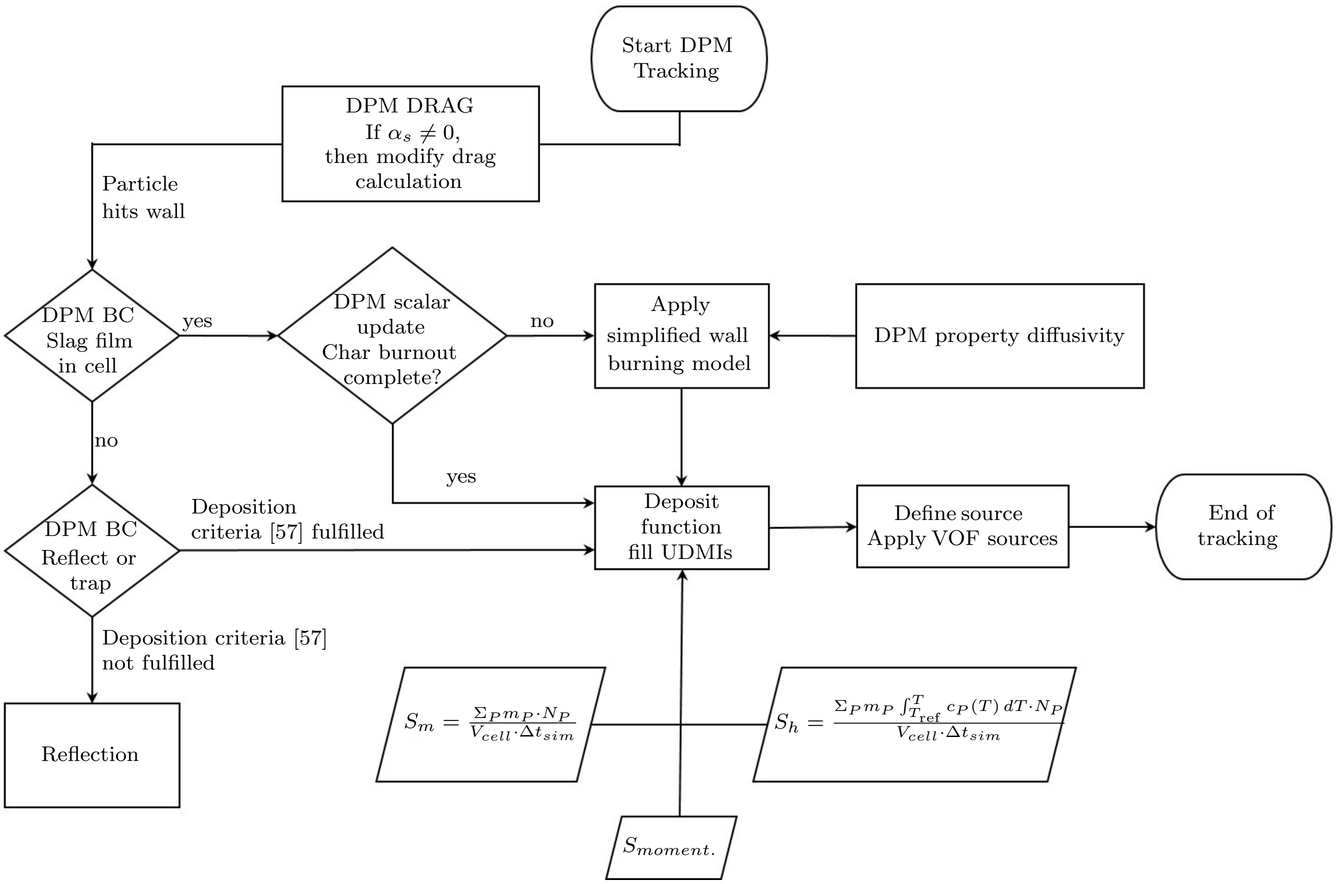

Figure 3: Modified DPM tracking

Additionally, the particle momentum is transferred to the slag phase, and UDMs are used to apply source terms accordingly.

Another key modification in this study was the implementation of a geometric viscosity average across the gas-slag interface to improve the prediction of momentum transfer. As illustrated in Fig. 4, the default setting in *Fluent* uses an arithmetic average. However, due to the high viscosity ratio between gas and slag, this method would assign a viscosity of 0.15 $Pa \cdot s$ for a typical interface cell with a slag volume fraction of 0.5, leading to inaccurate results. The recommended harmonic average, while more precise, introduced instabilities and required prohibitively small time steps. As a compromise, a geometric average was adopted, yielding a viscosity of 0.004 $Pa \cdot s$ for a typical interface cell. This approach offered the best balance between computational stability and accuracy.

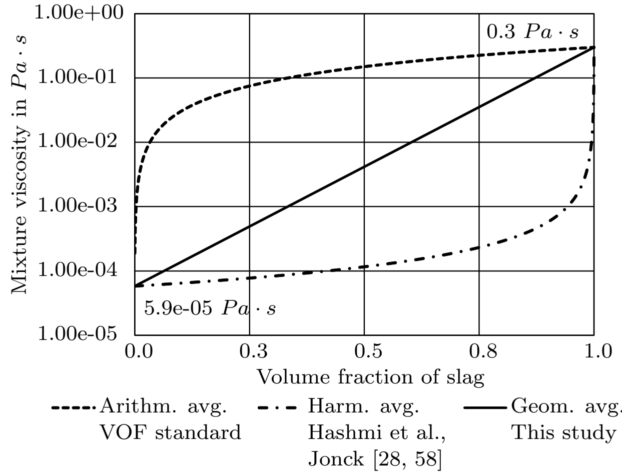

Figure 4: Viscosity averaging across gas-slag interface

3.3.3. EWF modeling

The VOF model is not compatible with non-premixed combustion models in Fluent [40]. A computationally inexpensive alternative is the EWF model, which can be used to model thin liquid films [18, 59]. The solution is performed in local coordinates parallel to the surface, without fully resolving the slag flow in 3D. The conservation of slag film thickness Eq. (25),

$$\frac{\partial \rho_s D}{\partial t} + \nabla_s \cdot (\rho_s D \vec{v_s}) = \dot{m}_s \tag{25}$$

in which ∇_s is the surface gradient operator, $\vec{v_s}$ the mean film velocity and $\dot{m}_s$ the mass source per unit wall area due to particle deposition, is solved with source terms generated from the DPM-deposition rate result (see also Fig. 5d). Similarly, in the conservation of momentum Eq. (26), $\vec{q_s}$ is applied.

$$\begin{aligned} \frac{\partial \rho_s D \vec{v_s}}{\partial t} + \nabla_s \cdot \left(\rho_s D \vec{v_s} \vec{v_s} + \vec{D_V} \right) &= -D \nabla_s P_L \\ + \rho_s D \vec{g} + \frac{3}{2} \vec{\tau_f}_s - \frac{3 \mu_s}{D} \vec{v_s} + \vec{q_s} + \vec{\tau_{\theta_w}} \end{aligned} \tag{26}$$

Therein $P_L = P_{gas} - \rho D(\vec{n} \cdot \vec{g}) - \sigma \nabla_s \cdot (\nabla_s D)$ includes the effects of gas flow pressure, gravity component normal to the wall (spreading) and surface tension. Further, $\vec{\tau_{\theta_w}}$ is the surface force due to film liquid surface tension and contact angle. $\rho_s D \vec{g}$, the main driving force, is the gravity component parallel to the film. To derive the shear and viscous terms on the right side of Eq. (26), a quadratic film velocity profile has been assumed [40]. The differential advection term $\vec{D_V}$ is also calculated on this basis. This limits the EWF approach, e.g., regarding solidification, which is often approximated using temperature-dependent viscosities. Temperature gradients across the film would result in a non-quadratic velocity profile and are thus not representable using the EWF approach. The conservation of energy is given with Eq. (27) in which T_f is the average film temperature:

$$\frac{\partial \rho_s D T_f}{\partial t} + \nabla_s \cdot \left(\rho_s D T_f \vec{v_s} + \vec{D_T} \right) = \frac{1}{c_p} \left[\frac{2k_f}{D} (T_s + T_w - T_m) + \dot{q_{imp}} \right] \tag{27}$$

Here, the differential advection term $\vec{D_T}$ and T_m (half-depth temperature) are also calculated based on quadratic film temperature profiles. $\dot{q_{imp}}$ is calculated from the droplet enthalpy analogous to the mass source term. c_p is the specific heat of the melt, k_f its thermal conductivity. T_s, and T_w are the film surface- and wall temperature.

The particle capture criteria (Tab. 4) is unchanged.

3.4. Computational domain and mesh independence

The mesh used for the EDM/VOF model is depicted in Fig. 1. Due to the model's complexity, it is divided into four parts, which are the main reaction zone, the burner, the phase separator zone and the flue gas outlet duct. The implementation of the burner was necessary to obtain realistic injection behavior which is influenced by the geometry upstream of the main reaction zone. The phase separator and flue gas duct regions are considered to obtain realistic outflow boundary conditions, which could not be achieved when the model was cut at the interface between the main reaction zone and the phase separator (swirling flow at the outlet, with non-uniform radial pressure distribution).

To resolve the slag flow, the mesh was refined close to the furnace walls, where the height of the first cell was approximately 0.01 mm. This is orders of magnitude lower than the estimated slag film thickness (see section 3.3). The region close to the walls had to be meshed using hexahedral cells since automatically generated, polyhedral meshes could not provide the necessary quality, especially in the sharp corners of the geometry. The mesh was further refined in several steps, close to the burner, and in locations with high-velocity gradients, e.g., regions influenced by the jets from the nozzles. This led to a final number of 5,122,245 cells. The minimum orthogonal quality is 9.4e-02.

During mesh-independence tests, it was observed that even after numerous iterations, the solutions exhibited slight oscillations, suggesting that the flow is (to some degree) inherently transient. As a result, direct comparisons

Table 5: Mesh independence investigation; wall resolution = number of cell layers at the wall (Fig. 1)

	coarse	medium	fine
Wall resolution	3	10	60
Cell count	1,749,384	2,163,595	5,122,245
Average swirl (m/s)	6.2	6.2	6.1
Integral deposition rate (kg/h))	75.2	54.0	53.5

of velocity profiles were considered less meaningful. Instead, to ensure accurate slag flow predictions, the focus shifted to evaluating time-averaged flow characteristics and deposition rates as the key metrics for determining sufficient mesh resolution. With Tab. 5, a comparison of the average swirl velocity, which is defined as the area-weighted average at the outlet of $\sqrt{u^2 + v^2}$ and the deposition rate integrated all over the furnace wall is given. Clearly, the mesh resolution did not significantly affect the main flow pattern, but had an impact on the amount of deposited slag, so the medium mesh was used for the SFM/EWF simulation. For the EDM/VOF model, the application of the fine mesh was necessary to resolve the slag layer.

3.5. Solution procedure

Both slag flow models are started from a converged steady-state solution for the particle-laden reactive flow. The steady-state solution is obtained using the following steps: First, the oxidizer flow only is solved, using the coupled solver, without the consideration of the discrete phase particles. This is done with the wall temperature set to 1550°C, which is an estimate from a conventional combustion calculation. After the swirling flow is developed, the DPM model is activated with a limited number of tracking steps, as small particles could get trapped in (re-)circulations, leading to instabilities, especially due to high particle-radiation interaction related source terms. The tracking steps are increased gradually, while the DPM under relaxation had to be decreased significantly. The DPM tracking starts at the air inlet surface, approximately 0.5 m above the injection to the hot reaction zone. This is done to allow for a realistic particle distribution at the reactor entrance. A total of 14 size classes adequately represent the PSD in the computational model, with particles larger than 500 µm being excluded. In total, around 30,000 particle tracks are considered within the steady-state simulation. Increasing this number did not change the results. In the transient simulation, particles have to be injected at a separate particle time step of 0.005 s to keep the flow- and temperature field steady. In total, around 36,000 particles are injected per time step and 105,000 are tracked in-flight within the domain.

Once the flow field is established, the 1550°C wall boundary condition is replaced with a mixed thermal boundary condition (internal $\epsilon = 0.9$, external $\epsilon = 0.6$, $h = 15\ W/(m^2 \cdot K)$, wall thickness 0.319 m, thermal conductivity (wall) = 1.0 $W/(m \cdot K)$). After the steady-state solution is reached, the slag models are loaded. A time-step of 1 second is used to keep the CFL number for the slag flow below one in most of the domain. This increment is too large to resolve most transient characteristics of gas phase combustion simulation, so the gas-phase solution is barely affected by this URANS approach. The implicit VOF formulation is used. The interface is captured using an accurate compressive scheme. For all other variables, second order upwind schemes were used. Pressure-velocity coupling is switched to SIMPLE during the transient calculation.

4. Results and discussion

This section presents the general flow field derived from the steady-state solution. The results from both the EDM and SFM models are discussed, followed by a comparison of the transient slag flow evolution for each model.

4.1. Flow field

Fig. 5 demonstrates the overall agreement between the EDM- and SFM-based models. In Fig. 5a the velocity magnitude in the zx-plane is shown, with white direction vectors included to clarify the flow directions. Predictably, the burner nozzles generate high velocity gradients near the burner and induce swirling flow within the reactor. Both models closely align in their predictions of the flow pattern. At the transition to the phase separator, both models predict a velocity magnitude of 11 m/s, with a significant component of approximately 6 m/s directed normal to the zx-plane, driven by the swirling flow.

Fig. 5b shows the temperature field results for both models, which are consistent with an outlet temperature of approximately 1550 °C. Minor differences are observed near the burner, but overall, the temperature distribution in the reactor is quite homogeneous due to effective insulation and even distribution of fuel and oxidizer around the reactor's circumference. Fig. 5c illustrates particle tracks colored by the char fraction, indicating that the burner jets direct particles toward the wall soon after injection. As a result, not all char is consumed before hitting the wall, particularly for larger particle fractions. This required the implementation of a wall-burning subroutine (see Fig. 3) in the model. Note, that the particle tracks are limited to a residence time of 0.3 seconds for visibility reasons. The burnout of the particles depends on the O_2 concentration and so the SFM model predicts a slightly slower burnout since the gas-phase reactions seem to occur faster (O_2 is consumed faster) and closer to the burner. Nevertheless, the resulting deposition rates in Fig. 5d demonstrate very close agreement between the models. The integral deposition rate over the surface area is 54 $kg/(m \cdot s)$ for both models, corresponding to approximately 63%

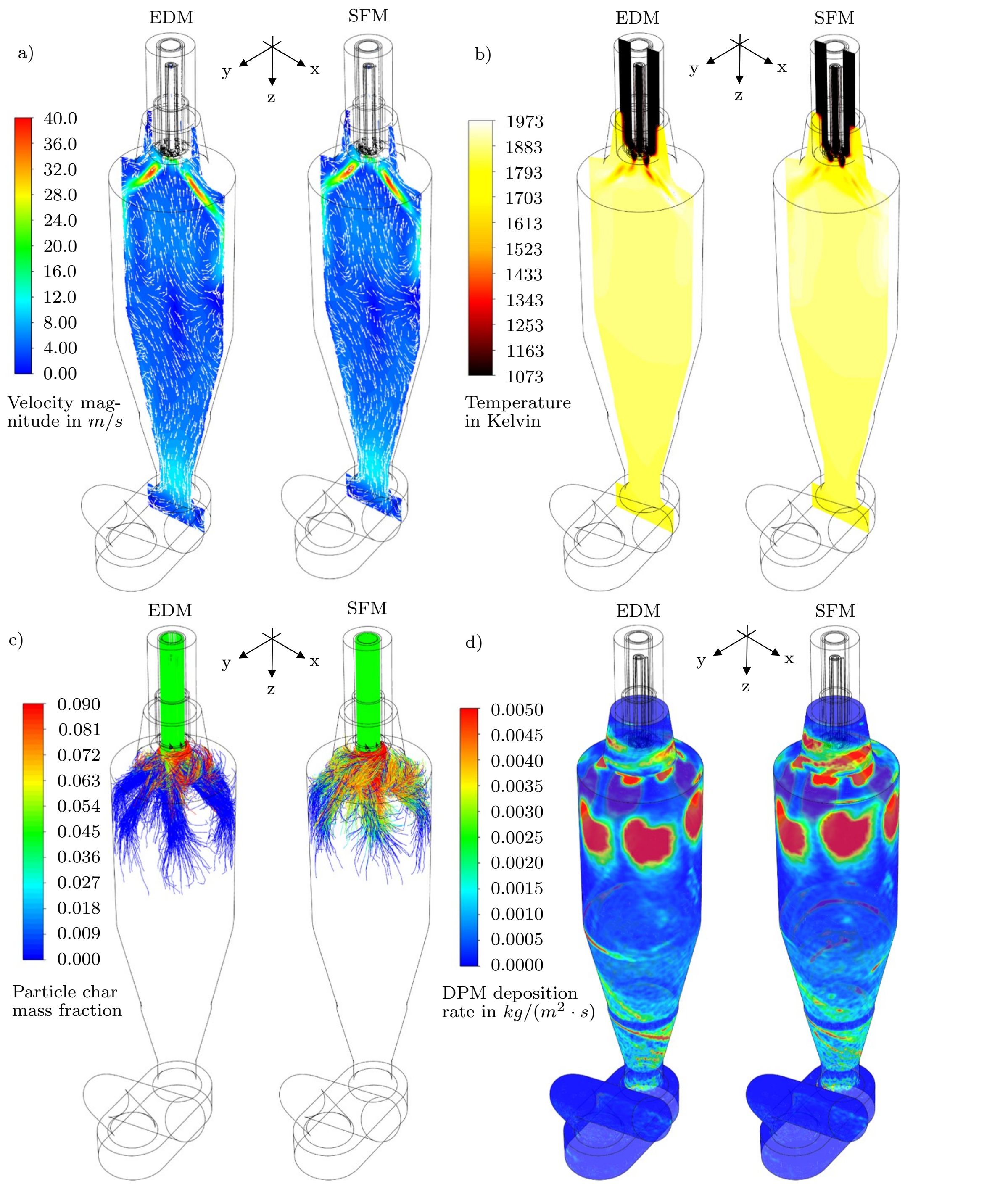

Figure 5: Comparison of main EDM and SFM model results - a) Velocity fields, b) Temperature fields, c) Particle tracks colored by the char mass fraction d) DPM deposition rates at the furnace walls

of the slag delivered through particulate matter after the organic material has evaporated or combusted. Note that also the remaining CaO from reaction (1) is counted to the slag. Fig. 5d already gives away that there also is a significant slag formation above the entrance to the reaction zone.

4.2. Slag flow predictions

This section presents and discusses the model predictions for both the EDM/VOF and SFM/EWF approaches. For each variant steady-state solutions serve as the initial conditions for the transient slag flow simulations in the furnace.

4.2.1. EDM/VOF

In Fig. 6a, the transient evolution of the liquid slag film is shown. The time stamps increase from left to right, starting at 16 seconds after the VOF model was activated and the transient simulation was started. The local distance from the wall, e.g., the variation of the thickness of the film, in mm, is indicated using the color bar. It becomes clear that the slag flow starts from the locations already indicated by the deposition rate predictions shown in Fig. 5d. This is a result of the burner configuration that features six lances which accelerate particles/droplets toward the wall in the upper cylindrical section of the reactor. Due to internal recirculation in the center of the reactor (Fig. 5a), but also close to the side wall, some particles are carried upwards by the flow against gravity and are deposited in the upper section of the reactor, even above the location of injection. This is why significant amounts of slag are appearing on the roof and burner housing walls. After about 100 seconds, the effect of gravity is showing and the slag collected at the wall starts to flow downward.

Although the deposition pattern after 16 seconds indicates some influence of the swirling gas flow in the lower conical section, this effect is primarily due to the particle deposition characteristics. As shown by comparing snapshots at 50 and 100 seconds, the slag consistently follows a downward flow pattern. After approximately 500 seconds, nearly the entire inner wall surface is covered by a film of molten slag. A statistically steady state is achieved after around 1000 seconds of process simulation time, at which point the maximum slag film thickness is predicted to be about 1.0 mm in the lower cylindrical section of the furnace. The maximum velocity in this region is predicted at 37 mm/s. The majority of the domain exhibits a slag thickness of around 0.6 mm and lower, with velocities around 15 mm/s. The higher maximum velocity predicted by the CFD model may result from increased shear between phases due to the geometric average and the non-uniform slag distribution around the furnace's circumference. Nonetheless, the average predictions align remarkably well with the analytical estimate discussed in section 3.3. The total slag mass distributed across the inner furnace surface is approximately 6 kg. The jet-induced deposition pattern is evident around the furnace's circumference and extends toward the bottom, where slag would drip into the phase-separator zone. The effect of dropping and collection in the tundish was not included in this

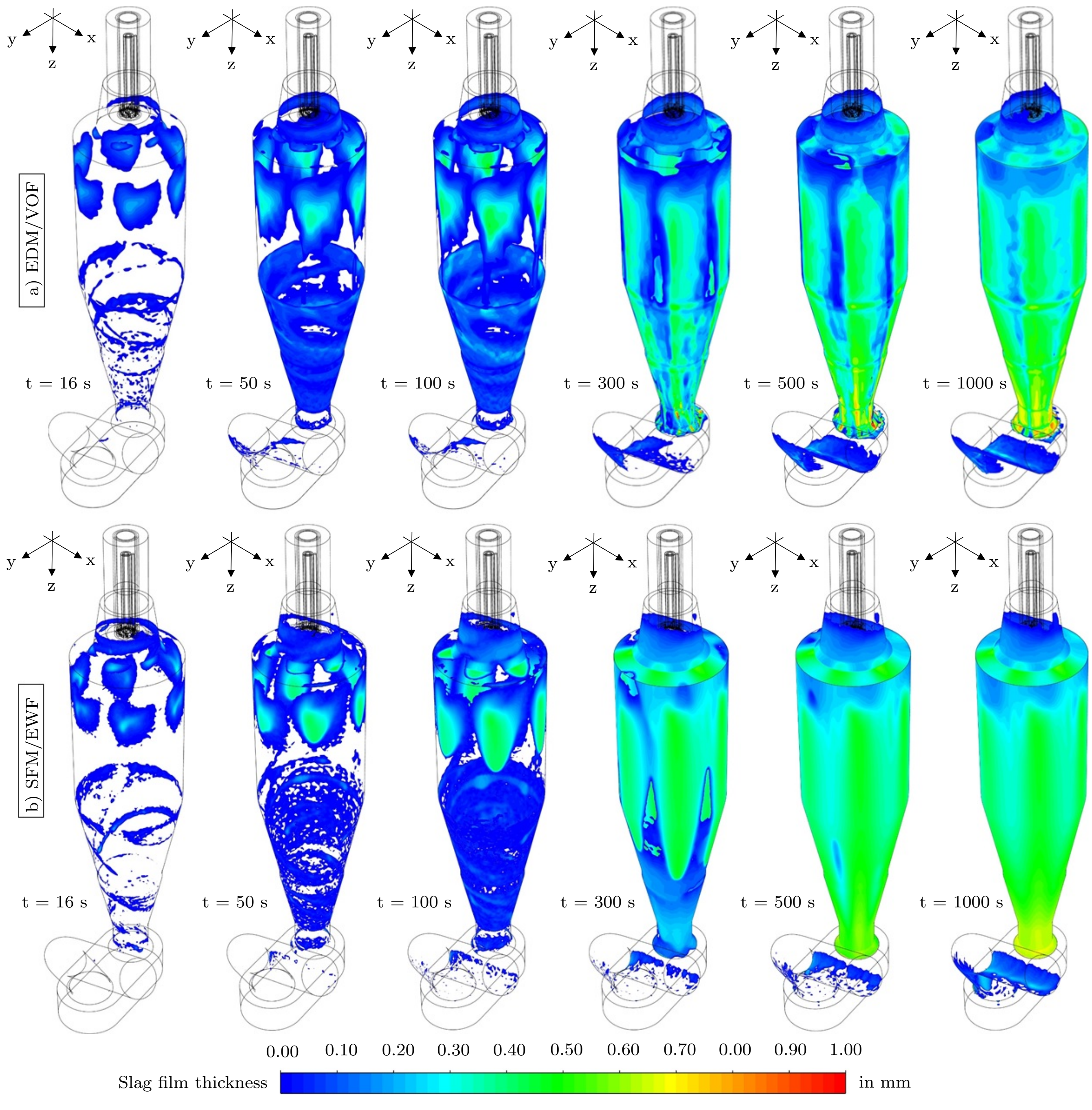

Figure 6: Transient evolution of slag film as calculated using a) the EDM/VOF model and b) the SMF/EWF model

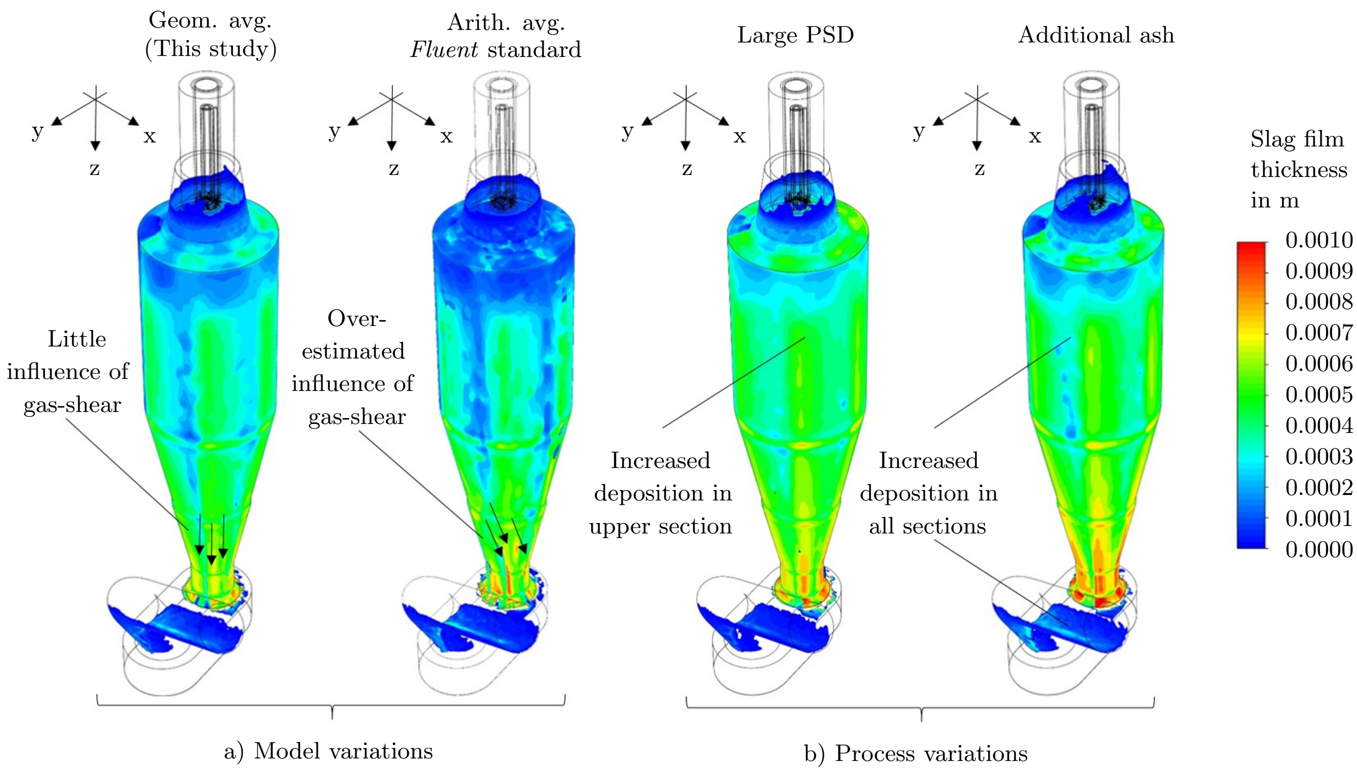

Figure 7: Case studies showing a) the difference between geometric- and arithmetic viscosity averaging and b) Case studies showing the result for an alternative PSD (left) and a process intensification case with a by 50% increased amount of ash injected for melting (right)

simulation as noted in section 3.3.

It is important to note that the standard VOF model, which uses an arithmetic average to calculate the mixture viscosity, tends to over-predict the influence of gas shear on slag motion. This can lead to inaccurate predictions of momentum transfer across the interface, as highlighted by [60]. Although the harmonic average recommended by Hashmi et al. [58] and implemented by Jønck [28] was considered, it introduced instabilities and required small time steps. Therefore, a geometric average as illustrated in Fig. 4 was employed in this study. Fig. 7a demonstrates the impact of these averaging methods. The arithmetic averaging method (right hand side) predicts a significant increase in motion influenced by the swirling gas flow, particularly in the lower part of the furnace, as indicated by the black arrows. In contrast, the model using the geometric viscosity average displays a much smoother and more vertically oriented slag flow.

As mentioned in section 2, the influence of the PSD was also investigated. The results are shown in Fig. 7b (left). Compared Fig. 7a (left), where the standard PSD with a size parameter of $x' = 52.6e-06$ m was used, here an increased x' of $142.6e-06$ m was considered. In general, the pattern is similar. There is a distinct influence of the burner, so depositions in the upper sections are present as well. This is because small particle fractions are always included, even if the overall particle sizes are larger. However, the results indicate that the increased inertia of the larger particles leads to a greater deposition rate in the upper part of the Flash reactor, as well as increased film thickness in this region and at the cylindrical outlet. Overall, the integral deposition rate in the furnace is higher with the larger particles, resulting in reduced carry-over. This has implications on the slag occurrence in the outlet section of the reactor, visible as lower film thickness in the outlet part of the system in Fig. 7b (left) compared to the standard case. Thus, the PSD has a significant impact on the expected flow of slag. Moreover, the reactor system allows the possibility of melting additional ash to increase the overall slag output. The right hand side of Fig. 7b presents a hypothetical process intensification case, in which additional ash is injected together with the unchanged amounts of sewage sludge and limestone. In total, this leads to a 50% increased slag occurrence. In contrast to the case with a larger PSD, this leads to increased depositions and slag flow in all sections of the reactor, including the outlet duct.

Fig. 8 provides a detailed view of the slag volume fraction in the furnace, again in the zx-plane and focusing on the right-hand side of the wall. The slag layer, which is barely visible in the full-scale view, is enlarged in the bottom subfigure for clarity. This enlargement reveals a sharp phase boundary, achieved through the compressive discretization scheme, which allows to avoid excessive mesh refinement at the gas-slag transition zone. The film in this location is about 0.6 mm thick. The central subfigure illustrates the velocity field with vectors scaled by the velocity magnitude. The profile near the wall is quadratic, consistent with the analytical solution. The contour is capped at 20 mm/s to highlight the transition to the gas phase, where the velocity significantly increases to around 11 m/s (see Fig. 5a). A velocity profile closely aligning with the theoretical prediction in section 3.3.1 is observed. The top subfigure, similar to Chen's study [24], shows that the thin slag layer exhibits a minimal temperature gradient, with the contour limits being only 0.5 K apart. This suggests that the slag layer does not significantly impact heat transfer in the furnace. Consequently, the heat loss of approximately 50 kW through the side walls was not notably changed compared to the steady-state simulation. The temperature contour is capped, with the far-field gas phase temperature at approximately 1820 K (1547°C).

In summary, the EDM/VOF approach offers a detailed, though computationally intensive, method for predicting slag flow in this setup. The complexity arises from the intricate interactions between gas jets, particle trajectories, and the resulting slag flow. The results shall now serve as a benchmark for the evaluation of the computationally inexpensive alternative.

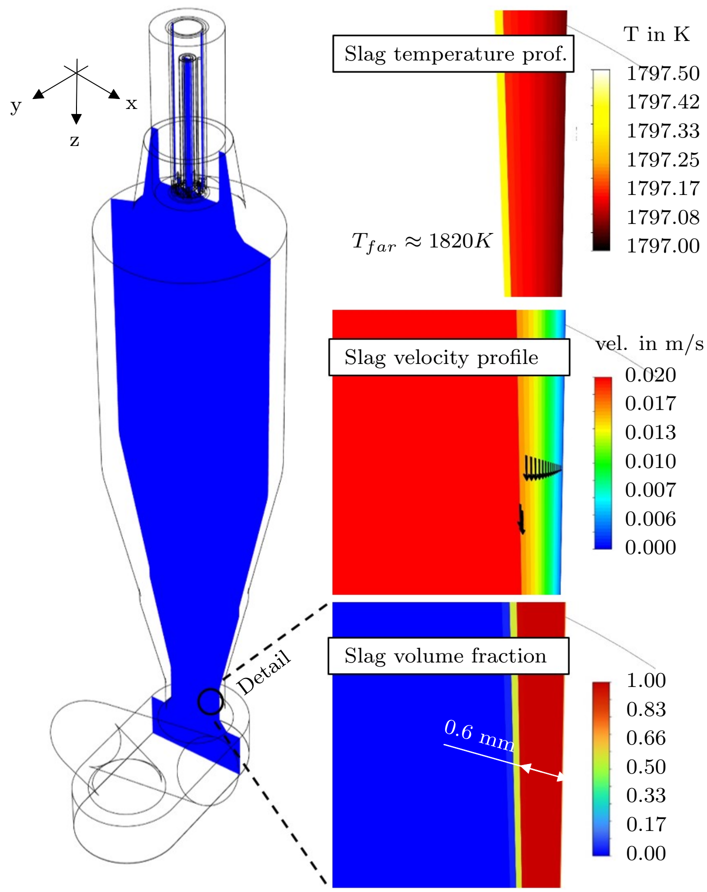

Figure 8: Detailed view on the slag layer at the wall of the furnace, showing temperature, velocity and phase fraction at the interface zone

4.2.2. SFM/EWF - Computationally inexpensive alternative

Through the case studies presented in Fig. 7b, it was noticed that the increased amount of slag and the alternative PSD do influence the deposition and flow characteristics, but not to a great extent. This is why the performance of the computationally inexpensive alternative shall be evaluated based on the standard case, however including the transient behavior. The slag flow prediction results of the SFM/EWF approach are shown in Fig. 6b. The spatial variation of the slag thickness is indicated using the same color scale as for the EDM/VOF model. The process time of the snapshots is also the same as above and starts at 16 seconds, increasing toward the right-hand side of Fig. 6b.

In close accordance with the resolved approach, the slag film starts to evolve in the upper section of the cylindrical reactor part. Since the locations of high deposition rates in Fig. 5d are predicted slightly higher than by the EDM-based model, the slag film also starts to develop at a higher vertical position. Furthermore, a significant portion of the slag is distributed across a broader area of the circumference, as indicated by the extensive regions with elevated deposition rates in Fig. 5d, including the roof. This smearing effect may be further exacerbated by the absence of wall-normal resolution in the EWF. Nevertheless, the magnitudes and thickness predictions are in close accordance with the detailed model. At around 100 seconds of process time, the vertical flow pattern of the slag motion starts to show. The depositions at the reactor roof and burner zone are also present and in the same order of magnitude.

At around 500 seconds, the entire surface is covered, but it takes again roughly twice that time to reach a steady state of operation. The magnitude of film thickness and velocity is in agreement with the EDM/VOF model (see Fig. 6a). The location where these maxima are to be found is the lower cylindrical part toward the phase separator section of the reactor. The total amount of slag is predicted slightly higher at around 6.5 kg, likely due to the even smaller influence of the gas shear. The SFM/EWF and EDM/VOF approaches also largely agree on the amount of slag occurring at the outlet duct, clearly showing a film concentrated on the bottom part of the outlet pipe, causing backward flow of slag in this region, where the temperatures are still hot enough to prevent solidification.

In summary, the results are of a very similar quality to those predicted by the film-resolving EDM/VOF approach. However, the required computation time to reach a statistically steady solution is significantly lower for the SFM/EWF model. This is because only 10 transport equations have to be solved here compared to the EDM/VOF approach with 15 equations (continuity, x-, y-, z-velocity, 2x turbulence, energy, radiation, 6x species plus VOF). Additionally, the mesh size is smaller, since the fine boundary layer resolution can be omitted. From starting the steady-state EDM simulation to a converged result took approximately 48 hours (two full days) on a workstation with 16 CPUs and 128 GB of RAM. From there to the final transient VOF results another 790 hours (33 full days) were required. However, in the author's experience, this can vary since the interaction between the DPM model, especially with particle-radiation interaction requires an increased level of attention. In contrast, the steady-state SFM result is reached in approximately 18 hours, and the transient result required another 24 hours of computation time. In summary, the result was obtained in less than 2 days. Additionally, the solution process of the inexpensive model has proven to be much more stable and requires less attention than the film-resolving approach. It should also be kept in mind that the very fine wall mesh necessary for resolving the slag flow requires significantly more pre-processing effort.

5. Conclusions and outlook

Two different models for the inclusion of slag flow dynamics in the CFD simulation of sewage sludge combustion have been implemented. The sophisticated yet computationally demanding EDM/VOF model was applied in this context for the first time on a complex geometry and compared to a novel SFM/EWF approach. This was necessary since experimental data is exceptionally difficult to obtain in systems with such harsh, chemically aggressive and high-temperature conditions. Both modeling variants agree on the transient evolution of the slag flow inside an experimental pilot furnace developed as a part of a phosphorus recovery process.

The maximum values of film thickness and velocity were predicted at around 0.6 - 1.0 mm and 37 mm/s respectively by both models, which is in very good accordance with analytical estimates. The temperature gradient in the slag film is practically non-existent and its influence on the heat transfer characteristics is negligible. A significant influence of gas shear was not observed, regardless of the modeling concept, which is attributed to the high viscosity- and density ratio between liquid and gaseous phases. The correct description of this required an implementation of geometric viscosity averaging at the interface between the gas- and slag phase, which is not standard in the VOF model. The cases with alternative PSD and additional ash have shown a considerable effect on the slag flow amount, but not on the general pattern.

Each modeling approach presents distinct advantages and drawbacks. The EDM/VOF approach is capable of resolving the slag film directly and is thus extendible to include solidification effects, which are the basis for the consideration of freeze linings. It is however limited to relatively simple chemical kinetics for the gas phase. The main disadvantage is the computational demand, not only regarding computation time but also regarding the requirement for fine and high-quality meshes at the walls where slag film formation is expected. The proposed SFM/EWF model is significantly easier to handle, has less demanding mesh requirements and is significantly faster to solve. A statistically steady solution can be obtained in less than 2 days compared to at least 35 days for the detailed modeling approach. However, as the SFM/EWF approach assumes quadratic film velocity profiles, it does not allow viscosity variations normal to the wall, e.g., through solidification, it is limited in this regard. For such cases, detailed modeling remains indispensable.

In summary, both models constitute efficient tools for further research and development but also for the efficient application in the engineering process of entrained flow furnaces. These can be an important part of phosphorus recovery processes, that aim to recover phosphorus from ash/slag.

Declaration of competing interest

The authors declare that they have no known competing financial interests or personal relationships that could have appeared to influence the work reported in this paper.

Acknowledgements

This project has received funding from the European Union's Horizon 2020 research and innovation programme under grant agreement No 958267.

Disclaimer

This publication reflects only the authors' views, and the European Health and Digital Executive Agency (HaDEA) and the European Commission are not responsible for any use that may be made of the information it contains.

References

[1] European Commission. *Report on critical raw materials and the circular economy.* Brussels, 2018.

[2] European Commission. *Critical Raw Materials Resilience: Charting a Path towards greater Security and Sustainability.* Brussels, 2020.

[3] Flash Phos Consortium. Flashphos: The complete thermochemical recycling of sewage sludge, 2020.

[4] A. Bianchini, L. Bonfiglioli, M. Pellegrini, and C. Saccani. Sewage sludge management in europe: a critical analysis of data quality. *International Journal of Environment and Waste Management*, 18(3):226, 2016.

[5] M. Atienza-Martínez, G. Gea, J. Arauzo, Sascha R.A. Kersten, and A. Maarten J. Kootstra. Phosphorus recovery from sewage sludge char ash. *Biomass and Bioenergy*, 65:42–50, 2014.

[6] N. Gao, K. Kamran, C. Quan, and P. T. Williams. Thermochemical conversion of sewage sludge: A critical review. *Progress in Energy and Combustion Science*, 79:100843, 2020.

[7] S. Arnout, A. Kotze, E. Nagels, Y. Cryns, and D. Messina. Flashphos: Elemental phosphorus recovery from sewage sludge - raw material thermal behaviour. *Prceedings of the EMC*, 2023.

[8] J. Werther and T. Ogada. Sewage sludge combustion. *Progress in Energy and Combustion Science*, 25(1):55–116, 1999.

[9] T. Ogada and J. Werther. Combustion characteristics of wet sludge in a fluidized bed. *Fuel*, 5(75), 1996.

[10] H. Cui, Y. Ninomiya, M. Masui, H. Mizukoshi, T. Sakano, and C. Kanaoka. Fundamental behaviors in combustion of raw sewage sludge. *Energy & Fuels*, 20(1):77–83, 2006.

[11] A. Žnidarčič, T. Seljak, and T. Katrašnik. Surrogate model for improved simulations of small-scale sludge incineration plants. *Fuel*, 280:118422, 2020.

[12] A. Žnidarčič, T. Katrašnik, I. G. Zsély, T. Nagy, and T. Seljak. Sewage sludge combustion model with reduced chemical kinetics mechanisms. *Energy Conversion and Management*, 236:114073, 2021.

[13] B. Ortner, C. Schmidberger, H. Gerhardter, R. Prieler, H. Schröttner, and C. Hochenauer. Computationally inexpensive cfd approach for the combustion of sewage sludge powder, including the consideration of water content and limestone additive variations. *Energies*, 16(4):1798, 2023a.

[14] B. Ortner, C. Schmidberger, H. Gerhardter, R. Prieler, H. Schröttner, and C. Hochenauer. Application of computationally inexpensive cfd model in steady-state and transient simulations of pulverized sewage sludge combustion. *Advanced Powder Technology*, 34(12):104260, 2023b.

[15] B. Ortner, C. Schmidberger, H. Gerhardter, R. Prieler, and C. Hochenauer. Application of computationally inexpensive cfd approach for the combustion of sewage sludge powder in entrained flow furnaces. *Proceedings of the 14th European Conference on Industrial Furnaces and Boilers (INFUB-14)*, (ISBN: 978-989-35683-0-9), 2024.

[16] B. Ortner, C. Schmidberger, R. Prieler, V. Mally, and C. Hochenauer. Analysis of the shear-driven flow in a scale model of a phase separator: Validation of a coupled cfd approach using experimental data from a physical model. *International Journal of Multiphase Flow*, 177:104852, 2024.

[17] A. A. Bhuiyan and J. Naser. Modeling of slagging in industrial furnace: A comprehensive review. *Procedia Engineering*, 105:512–519, 2015.

[18] A. A. Bhuiyan, A. S. Blicblau, and J. Naser. Co-firing of biomass and slagging in industrial furnace: A review on modelling approach. *Journal of the Energy Institute*, 90(6):838–854, 2017.

[19] M. Seggiani. Modelling and simulation of time varying slag flow in a prenflo entrained-flow gasifier. *Fuel*, 77(14):1611–1621, 1998.

[20] P. J. Benyon. *Computatonal Modelling of Entrained Flow Slagging Gasifier*. Ph.d. thesis, University of Sydney, 2002.

[21] S.. Liu and Y. Hao. Numerical study on slag flow in an entrained-flow gasifier. *Proceedings of IMECE2007, ASME International Mechanical Engineering Congress and Exposition*, 2007.

[22] J. Xu, Z. Dai, H. Liu, L. Guo, and F. Sun. Modeling of multiphase reaction and slag flow in single-burner coal water slurry gasifier. *Chemical Engineering Science*, 162:41–52, 2017.

[23] C. Chen, P. Li, L. Chen., Y. Zhang, L. Zhang, and X. Yang. Simulation of deposition and flow characteristics of slag in entrained flow gasifiers. *Industrial & Engineering Chemistry Research*, 62(29):11666–11676, 2023.

[24] L. Chen. *Computational Fluid Dynamics Simulations of Oxy-Coal Combustion for Carbon Capture at Atmospheric and Elevated Pressure*. Ph.d. thesis, Massachusetts Institute of Technology, 2013.

[25] L. Chen and A. F. Ghoniem. Development of a three-dimensional computational slag flow model for coal combustion and gasification. *Fuel*, 113:357–366, 2013.

[26] A. A. Bhuiyan and J. Naser. Modelling of slag deposition and flow characteristics of coal combustion under oxy-firing condition in a 550 mw tangentially fired furnace. *Applied Thermal Engineering*, 106:221–235, 2016.

[27] A. A. Bhuiyan and J. Naser. Development of 3d transient wall filming mechanism during combustion by coupling eulerian-lagrangian approach and particle-wall interaction model. *Applied Thermal Engineering*, 112:911–923, 2017.

[28] K. M. Jønck. *CFD Modelling of Melting Cyclones for Stone Wool Production.* 2021.

[29] B. Ortner, C. Hochenauer, and C. Schmidberger. Flashphos: The complete thermochemical recycling of sewage sludge: Public deliverable 2.2, 2023.

[30] H. Gerhardter, M. Knoll, J. Raic, R. Prieler, M. Landfahrer, C. Hochenauer, P. Tomazic, and H. Schroettner. In-flame spheroid formation from non-spherical slag particles – a numerical and experimental study. *International Journal of Heat and Mass Transfer*, 151:119412, 2020.

[31] P. Rosin and Rammler E. The law governing the fineness of powdered coal. *Journal Inst. Fuel*, 7:109–122, 1933.

[32] P. A. Vesilind. The rosin-rammler particle size distribution. *Resource Recovery and Conservation*, 5(3):275–277, 1980.

[33] S. Vargas, F. J. Frandsen, and K. Dam-Johansen. Rheological properties of high-temperature melts of coal ashes and other silicates. *Progress in Energy and Combustion Science*, 27:237–429, 2001.

[34] T. H. Shih, W. W. Liou, A. Shabbir, Yang Z., and Zhu J. A new $k- \varepsilon$ eddy viscosity model for high reynolds number turbulent flows. *Computers & Fluids*, 24(3):227–238, 1995.

[35] Y. Wu, J. Zhang, P. J. Smith, H. Zhang, C. Reid, J. Lv, and G. Yue. Three-dimensional simulation for an entrained flow coal slurry gasifier. *Energy & Fuels*, 24(2):1156–1163, 2010.

[36] B. Mayr, R. Prieler, M. Demuth, and C. Hochenauer. The usability and limits of the steady flamelet approach in oxy-fuel combustions. *Energy*, 90:1478–1489, 2015.

[37] F. Edler, B. Geier, Wolfgang Reiter, R., Rieger, J., C. Spijker, and H. Raupenstrauch. Development of an atmosphere particle kinetic model for particle reactions in a combustion flash-reactor using cfd- methods. *Energy Procedia*, 120:540–547, 2017.

[38] H. Gerhardter, R. Prieler, B. Mayr, M. Landfahrer, M. Mühlböck, P. Tomazic, and C. Hochenauer. Assessment of a novel numerical model for combustion and in-flight heating of particles in an industrial furnace. *Journal of the Energy Institute*, 91(6):817–827, 2018.

[39] G. Daurer, J. Raič, M. Demuth, C. Gaber, and C. Hochenauer. Detailed comparison of physical fining methods in an industrial glass melting furnace using coupled cfd simulations. *Applied Thermal Engineering*, 232:121022, 2023.

[40] ANSYS Inc ANSYS Fluent. *Theory Guide Release 2020 R2*. Canonsburg, PA, USA, 2020.

[41] H. A. Wadell. Volume, shape and roundness of rock particles. *The Journal of Geology*, 40(5):443–541, 1932.

[42] A. Haider and O. Levenspiel. Drag coefficient and terminal velocity of spherical and nonspherical particles. *Powder Technology*, 58(1):63–70, 1989.

[43] M. Knoll, H. Gerhardter, C. Hochenauer, and P. Tomazic. Influences of turbulence modeling on particle-wall contacts in numerical simulations of industrial furnaces for thermal particle treatment. *Powder Technology*, 373:497–509, 2020.

[44] M. Knoll, H. Gerhardter, P. Tomazic, and C. Hochenauer. Investigations of lateral particle distribution for spherical and highly non-spherical particles by means of steady-state/transient rans and les simulations. *Powder Technology*, 378:618–638, 2021.

[45] W. E. Ranz and W.R.J. Marshall. Evaporation from drops. *Chemical Engineering Progress*, 48(3):141–146, 1952.

[46] H. Gerhardter, R. Prieler, C. Schluckner, M. Knoll, C. Hochenauer, M. Mühlböck, P. Tomazic, and H. Schroettner. Modelling convective heat transfer to non-spherical particles. *Powder Technology*, 343:245–254, 2019.

[47] R. Cai, K. Luo, H. Watanabe, R. Kurose, and J. Fan. Recent advances in high-fidelity simulations of pulverized coal combustion. *Advanced Powder Technology*, 31(7):3062–3079, 2020.

[48] M. Knoll, H. Gerhardter, R. Prieler, C. Hochenauer, P. Tomazic, and H. Schröttner. Effects on numerical calculations of in-flight particle trajectories and temperatures considering multiple particle size and shape. *International Journal of Thermofluids*, 7-8:100021, 2020.

[49] M. F. Modest. *Radiative heat transfer*. Academic Press, New York, 3. ed. edition, 2013.

[50] G. D. Raithby and E. H. Chui. A finite-volume method for predicting a radiant heat transfer in enclosures with participating media. *J. Heat. Transf*, 112:415–423, 1990.

[51] H. C. Hottel and A. F. Sarofim. Radiative transfer. *McGraw-Hill Book Company*, 1967.

[52] T. F. Smith, Shen F., and Friedman N. Evaluation of coefficients for the weighted sum of gray gases mode. *J. Heat Transfer*, 104:602–608, 1982.

[53] S. Badzioch and P. G. W. Hawksley. Kinetics of thermal decomposition of pulverized coal particles. *Industrial & Engineering Chemistry Process Design and Development*, 9(4):521–530, 1970.

[54] B. F. Magnussen and B. H. Hjertager. *On mathematical modeling of turbulent combustion with special emphasis on soot formation and combustion*, volume 16. 1977.

[55] J. B. Howard, G. C. Williams, and D. H. Fine. Kinetics of carbon monoxide oxidation in postflame gases. *Symposium (International) on Combustion*, 14(1):975–986, 1973.

[56] M. Bui-Pham and K. Seshadri. Comparison between experimental measurements and numerical calculations of the structure of heptane-air diffusion flames. *Combustion Science and Technology*, 74(4):293–310, 1991.

[57] S. Z. Yong, M. Gazzino, and Ghoniem. Modeling the slag layer in solid fuel gasification and combustion – formulation and sensitivity analysis. *Fuel*, 92(1):162–170, 2012.

[58] A. A. Hashmi, K. Dullenkopf, R. Koch, and H.-J. Bauer. Cfd methods for shear driven liquid wall films. *Proceedings of the ASME Turbo Expo*, pages 1283–1291, 2010.

[59] E. Hashemian Nik, S. Pletzer, and C. Hochenauer. Numerically efficient two-step cfd simulation model of flow regime and heat transfer for hot water shower sterilizers. *Applied Thermal Engineering*, 230:120649, 2023.

[60] G. Chinello, Ayati, A. A., McGlinchey, D., G. Ooms, and R. Henkes. Comparison of computational fluid dynamics simulations and experiments for stratified air-water flows in pipes. *Journal of fluids Engineering, Transactions of the ASME 141.5*, 141(5), 2019.